

Quantitative nanoscale imaging using transmission He ion channelling contrast: Proof-of-concept and application to study isolated crystalline defects

Saba Tabean^{a,b}, Michael Mousley^a, Christoph Pauly^c, Olivier De Castro^a, Eduardo Serralta^{d,e}, Nico Klingner^d, Frank Mücklich^c, Gregor Hlawacek^d, Tom Wirtz^a, Santhana Esvara^a

^a Advanced Instrumentation for Nano-Analytics (AINA), Luxembourg Institute of Science and Technology (LIST), Materials Research and Technology Department, 41, rue du Brill, L-4422, Belvaux, Luxembourg

^b University of Luxembourg, 2 Avenue de l'Université, Esch-sur-Alzette L-4365, Luxembourg

^c Functional Materials, Department of Materials Science, Saarland University, D-66123, Saarbrücken, Germany

^d Institute of Ion Beam Physics and Materials Research, Helmholtz-Zentrum Dresden-Rossendorf, Bautzner Landstr. 400, D-01328 Dresden, Germany

^e Technische Universität Dresden, Dresden D-01069, Germany

A B S T R A C T

A newly developed microscope prototype, namely npSCOPE, consisting of a Gas Field Ion Source (GFIS) column and a position sensitive Delay-line Detector (DL) was used to perform Scanning Transmission Ion Microscopy (STIM) using keV He⁺ ions. One experiment used 25 keV ions and a second experiment used 30 keV ions. STIM imaging of a 50 nm thick free-standing gold membrane exhibited excellent contrast due to ion channelling and revealed rich microstructural features including isolated nanoscale twin bands which matched well with the contrast in the conventional ion-induced Secondary Electron (SE) imaging mode. Transmission Kikuchi Diffraction (TKD) and Backscattered Electron (BSE) imaging were performed on the same areas to correlate and confirm the microstructural features observed in STIM. Monte Carlo simulations of the ion and electron trajectories were performed with parameters similar to the experimental conditions to derive insights related to beam broadening and its effect in the degradation of transmission image resolution. For the experimental conditions used, STIM imaging showed a lateral resolution close to 30 nm. Dark twin bands in bright grains as well as bright twin bands in dark grains were observed in STIM. Some of the twin bands were invisible in STIM. For the specific experimental conditions used, the ion transmission efficiency across a particular twin band was found to decrease by a factor of 2.8. Surprisingly, some grains showed contrast reversal when the Field of View (FOV) was changed indicating the sensitivity of the channelling contrast to even small changes in illumination conditions. These observations are discussed using ion channelling conditions and crystallographic orientations of the grains and twin bands. This study demonstrates for the first time the potential of STIM imaging using keV He⁺ ions to quantitatively investigate channelling in nanoscale structures including isolated crystalline defects.

1. Introduction

Helium Ion Microscopy (HIM) has emerged as a versatile technique for nanoscale imaging [1], nanofabrication [2] and chemical analysis [3, 4]. The high brightness GFIS used in HIM allows a primary ion beam spot size of ~ 0.5 nm [1][1]. The He ion-solid interaction volume within the secondary electron (SE) escape depth is narrower than that of an electron beam of similar energy which results in a better lateral imaging resolution than conventional Scanning Electron Microscopy (SEM) [1]. Furthermore, in comparison to an electron beam, the higher stopping power of ions in solids and, in many cases, the lower contribution from Type II SE electrons (i.e. those produced by backscattered particles leaving the sample) results in a majority of the SE signal originating from the surface, thereby resulting in superior imaging of the surface details compared to a SEM [1]. Moreover, the small spot size and large depth of field of HIM is also excellently suited for nanofabrication with a lateral resolution better than conventional Ga Focused Ion Beam (FIB)

instruments [5].

HIM imaging is primarily performed in the SE mode. Other imaging modes in a Helium Ion Microscope (HIM) using backscattered He particles [6,7], ionoluminescence [8], secondary ions [3,4,9] and transmitted He particles (ions and neutrals) [10] have also been demonstrated which bring complementary insights about the analysed material. In this context, several groups have recognized the relatively unexplored potential in the use of transmitted He particles for advanced imaging modes. Transmission ion microscopy (TIM) allows the possibility to localise and image sub-surface features, to reveal information on the crystalline nature of the sample [11] and can also be very helpful in metrology and other applications, for instance in semiconductor fabrication [12].

Whilst TIM is similar to transmission electron microscopy (TEM) there are several advantages of using ions. Charge exchange processes are not visible in a TEM for the simple reason that electrons are absorbed by the material and subsequently are not available for imaging, the

<https://doi.org/10.1016/j.ultramic.2021.113439>

Received 22 June 2021; Received in revised form 19 November 2021; Accepted 27 November 2021

Available online 1 December 2021

0304-3991/© 2021 The Author(s). Published by Elsevier B.V. This is an open access article under the CC BY license (<http://creativecommons.org/licenses/by/4.0/>).

information is lost. However, when using ions, the neutral signal can be recorded, preserving the information about the fraction of neutralisation and the location of neutralisation on the sample. These charge exchange processes will be important when producing contrast with low Z materials, such as biological samples. Secondly, ion channelling is sensitive to whether dopant atoms are in interstitial or substitutional sites, such investigations are difficult in a TEM. In addition to this channelling sensitivity, ions have scattering cross sections orders of magnitude larger than electrons of the same energy, meaning lower doses can be used to achieve contrast on beam sensitive samples. One restriction for TEM is that samples must be generally conductive (thin insulating films adjacent to a conductive material can also be imaged by TEM), whereas an electron flood gun can be used during ion microscopy to counteract any charging, allowing even bulk insulating samples to be imaged. Finally, TIM can investigate fundamental aspects of ion-solid interactions, improving our understanding of basic physics, such studies are impossible in a TEM.

There are multiple methods used to detect a TIM signal, each with their own advantages and disadvantages. Early approaches to STIM in a HIM involved an indirect detection wherein the transmitted He particles impinge on a metal plate, SEs are thus produced, which are detected by the instrument's SE detector to generate STIM images while blocking most of the SEs from the sample surface[10,13]. An adaptation of this approach using an annular configuration was demonstrated for dark-field STIM imaging[10,14]. These SE based methods do not require any extra detectors and larger beam currents can be used compared to more sensitive detectors. However, one cannot measure counts directly and there is no positional information on the detector. In addition, extra measures are required to reduce the SE electron signal coming from the top of the sample[14]. A silicon diode array detector has also been used to detect transmitted ions with a stationary primary ion beam to detect scattered intensities on the detector plane[15,16] and a scanning beam for STIM imaging[17]. This diode array allows neutrals to be detected as well as ions and the image gives positional information of the counts on the detector, but one cannot record individual arrival times. STIM investigations in a HIM involving direct ion (and neutral) detection have also been reported, notably using an annular Micro Channel Plate (MCP) [18] for dark-field imaging and more recently in combination with a delay-line detector (DLD) to simultaneously obtain on-axis (bright-field) and off-axis (dark-field) data for STIM imaging[11]. The use of an MCP allows variable gain on the detector, increasing the range of intensities which can be imaged. In addition, the MCP can detect neutrals. The DLD is more expensive, however using a DLD system gives the possibility to perform more advanced imaging modes. This is because the DLD records positional information and the arrival time for each count, allowing post processing to select specific groups of counts from the 5 dimensional dataset (2D sample position, 2D detector position and arrival time). Apart from scanning mode imaging in a HIM, transmission ion microscopy using stationary broad-beam illumination of He⁺ with energies below 50 keV, has also been reported[19]. This used a detector with an MCP and a phosphor screen as well as an attenuation grid, allowing higher beam currents to be used whilst giving positional information, but there was no arrival time information.

The objective of the present article is to demonstrate, for the first-time, quantitative STIM imaging in HIM using a case study of isolated crystalline defects in thin polycrystalline gold membrane. A comparison of the contrasts in STIM and SE images is first presented and the lateral resolution of STIM images is determined experimentally and compared with beam broadening calculated using Monte Carlo simulations. Then, using a correlative approach combining STIM and electron diffraction on the same areas, we present a quantitative nanoscale analysis of transmitted He ions and neutrals through regions with and without crystalline defects.

2. Experimental methods

The sample was a 50 nm thick freestanding Au membrane (UltraFoil®, Quantifoil Micro Tools GmbH) on a 300 mesh Au grid which was annealed for 2 h at 700 °C to obtain large grains with isolated twin defects. The npSCOPE prototype[11,20] was used for STIM and SE imaging. It consists of a commercial GFIS ion column used in a HIM (Carl Zeiss SMT, Inc., Peabody, MA) and a custom-built large sample chamber equipped with a STIM detection setup to allow more advanced STIM imaging conditions which are not possible in a commercial HIM. In addition to the STIM mode, the npSCOPE prototype has an in-house designed magnetic-sector mass spectrometer to perform high-resolution chemical imaging using Secondary Ion Mass Spectrometry (SIMS)[9].

The STIM images apart from those in Fig. 1 were obtained using a 25 keV He⁺ primary ion beam passing through a 10 µm beam limiting aperture with spot control 5 setting and a helium pressure of 2.6×10^{-6} Torr. These conditions result in an estimated primary beam current of 0.05 pA on the sample, which helps to reduce ion beam damage to the STIM detector. The SE and STIM images in Fig. 1 were recorded in different conditions, with 30 keV primary ion beam voltage and spot control 4. These parameters lead to an estimated primary beam current of 0.5 pA on the sample for SE imaging with 2.6×10^{-6} Torr helium gas pressure and 0.1 pA for STIM imaging with 2.7×10^{-7} Torr helium gas pressure. The SE images were recorded using the Everhart-Thornley (ET) detector in a raster matrix of 1024×1024 pixels with frame average set to 8 and a dwell time of 20 µs per pixel. STIM images were obtained as a single frame scan with the same beam current but as a raster matrix of 512×512 pixels and a dwell time of 110 µs per pixel. For the STIM images presented in this article, the sample-to-detector distance was 256 mm corresponding to a scattering angle from 0 to 97 mrad for all azimuthal angles (and extending to 137 mrad on the corners of the detectors). The STIM detector including the DLD configuration is described in more detail elsewhere[11].

When an energetic He ion or neutral enters a channel of the MCP, SEs are produced and are then multiplied and subsequently hit the delay line structure and induce output signals. The arrival time of electrical pulses at the end of each delay line reveal the x and y coordinates of the location where each ion or neutral impact event occurred on the STIM detector. Finally, for every detected event the system is able to represent the 2D data set of positions on the detector, linking these events to the corresponding x, y raster locations of the primary beam on the sample resulting in a 4D dataset. The 4D datasets offer the possibility to construct STIM images using a user-specified range of scattering angles resulting in on-axis (or Bright-Field, BF) images and off-axis which may or may not produce a Dark-Field (DF) image depending on the scattering radius of ions from the sample, which is determined by chemical composition of the sample (which defines the scattering angle) and the sample-to-detector distance. Alternatively, the intensity distribution on the detector for a user-specified sub-section of a sample area is also possible (via post processing of the dataset) allowing the investigation of transmission characteristics of isolated features within an image. All the STIM images presented in this article are from such 4D datasets. When combined with a primary beam pulsing system, time-of-flight could also be added to the dataset resulting in 5D datasets.

Transmission Kikuchi Diffraction (TKD) was carried out in an FEI Helios Nanolab600 FIB/SEM equipped with a Schottky field emission gun and an EDAX Hikari Electron Backscatter Diffraction (EBSD) camera. The acceleration voltage was set to 30 kV to minimize the lateral scattering of the e-beam during transmission and a beam current of 5.5 nA was used. The SE mode image resolution for the FIB/SEM under these conditions was determined to be 4.8 nm on a tin ball calibration sample using edge profile analysis. For TKD, the sample stage was tilted so that the angle between incident electron beam and sample surface normal was 25°. When using classical EBSD detector geometries that are built for reflection rather than transmission measurements, this tilt angle can be

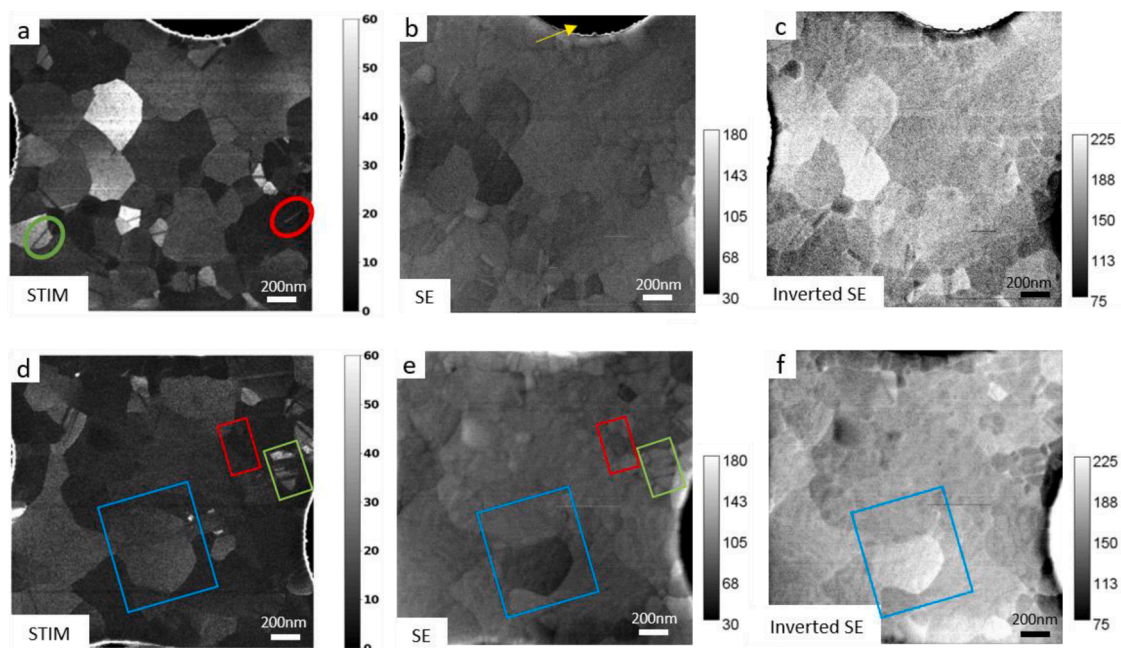


Fig. 1. STIM (a,d), corresponding SE (b,e) and SE with inverted contrast (c,f) image pairs of thin freestanding polycrystalline Au sample (thickness ~ 50 nm). The straight dark lines seen within some grains in the STIM images correspond to twin bands. Dark twin bands in a bright grain (green circle in figure a) and bright twin bands in a dark grain (red circle in figure a) are observed. The SE contrast, of the same ROI, has been inverted in figure c and f to highlight the inverse contrast between SE and STIM images. The same grain imaged in STIM and SE is indicated by a blue rectangle in (d,e). The rich details of the microstructure seen in the STIM mode are also visible to some extent in the SE mode. Some grains appear dark in both SE and STIM images indicated by red rectangles in (figure d and e) whereas some grains appear bright in both SE and STIM images indicated by green rectangles in (figure d and e). For colour images see the online version of this article.

varied to find a compromise between best lateral resolution (at normal incidence) and sufficient illumination of the EBSD camera screen (towards higher angles). In general, the spatial resolution of TKD depends on sample thickness and atomic number and thin samples comprising light elements yield best resolution because of minimal electron scattering inside the sample. Various authors have investigated the spatial resolution of the TKD technique. Depending on samples thickness and atomic number, values of 10 nm and less can be found in literature [21–23]. Measurements in the present study were carried out with different step sizes in the range of 5–7 nm using the software OIM Data Collection v7. Data analysis was done in EDAX OIM Analysis v7. At first, a grain confidence index (CI) standardization clean-up was performed followed by a CI filter to remove data points of a $CI < 0.09$. This step removes unreliable data points while not changing measured orientations. In a next step, each data set was rotated. It was found that the gold film was not perfectly flat but showed some warping. This became evident when plotting $\{111\}$ pole figures from the data of various regions of interest (ROI). The film exhibits a $\{111\}$ fibre texture, i.e. a strong pole in the centre of the $\{111\}$ pole figure and a ring formed by individual poles at 70.5° , the angle between planes of the $\{111\}$ family in the cubic lattice. The measured data, however, exhibited a deviation of the central pole from the centre of the pole figure which is a sign for local out-of-plane bending of the film. Rotating the dataset in OIM Analysis is a straightforward operation and was used to correct this deviation. Thus, it became possible to compare measured orientations between different ROIs. In a last step, a clean-up was performed to obtain a single average orientation per grain and individual grain orientations could be easily exported for further processing. Backscattered Electron (BSE) imaging was performed in the same microscope at 5 kV and a beam current of 86 pA in immersion mode using a solid state single-segment detector.

Monte Carlo simulations were carried out using parameters matching the experimental conditions to understand the consequences of ion-solid and electron-solid interactions and their contribution to the experimental results. The helium ion-solid interactions were simulated

using the freely available ‘Stopping and Range of Ions in Matter’ (SRIM) software [24]. The incident He^+ primary energy was set to 25 keV and the sample was a 50 nm thick Au membrane and the simulation type was set to ‘monolayer collision steps/surface sputtering’. The electron-solid interaction and electron transmission were simulated using the freely available CASINO software (V3.3.0.4) [25]. The electron energy was set to 30 keV, the beam diameter was set to 4.7 nm and the sample was defined as a 500 nm x 500 nm x 50 nm slab of Au. The simulation used the ‘Mott by equation (Browning 1994)’ physical model.

3. Results and discussion

A thin freestanding perforated polycrystalline gold membrane of thickness ~ 50 nm was imaged in STIM and SE imaging modes in a HIM. In Fig. 1(a–f), STIM images, the corresponding SE images and contrast-inverted SE images from two different ROIs are shown. The pixel values for the STIM images are direct numbers of counts, whereas the SE images are a mapping to a value between 0 and 255. The dark straight lines seen within certain grains in the STIM images correspond to twin bands as will be shown later. The twin bands appear dark (e.g. the green circle in Fig. 1a) because of the locally decreased ion channelling in comparison to the grain in which they are embedded. Bright twin bands in dark grains are also observed (e.g. the red circle in Fig. 1a). The dark semi circular features in STIM and SE images correspond to the periodic perforations in the gold film. They appear as dark disks in the SE images as expected (e.g. the yellow arrow in Fig. 1b). These same features are expected to appear as white disks in the STIM images. However, these disks appear dark in the STIM images because of the oversaturation of the DLD detector in these areas as the entire probe current is transmitted directly through these holes. The primary ion beam will hit a small area on the MCP detector which can locally not be recharged fast enough, leading to a severe decrease of the pulse height distribution below the noise level. Nevertheless, it can be seen from Fig. 1 that the variations in the extent of ion channelling from one grain to another manifest as contrast in the STIM images revealing rich microstructural details which

are also visible to some extent in the corresponding SE images. It is interesting to note here that most of the grains that are the brightest in STIM are the darkest in SE mode (see the blue rectangle in Fig. 1d, e and f). In order to highlight this, the pixel values and contrast parameters of the SE images were inverted, meaning the inverted image shows the difference between the original pixel value and 255 (see Figs 1c, f). Contrast ranges were set to the minimum and maximum of 75 and 225 respectively, whereas these parameters were set to 30 and 180 for the SE images (any pixel values outside these ranges are shown as the nearest colour, either black or white depending on if it is below or above the range respectively). The inverse relationship between the intensities in STIM and SE images for most grains is understandable as the grains that are favourably orientated for channelling will have lower secondary electron yield and hence appear dark in the SE image [26]. On the other hand, some grains appear bright or dark in both SE and STIM images. The dark contrast (e.g. the red rectangle in Fig. 1d and e) for both images could be the result of a change in orientation between two stacked grains. If the top grain is in an orientation favourable for channelling there will be a low SE yield and dark contrast in the SE image. Further travel of the He^+ ion through lower grains with a non channelling orientation could scatter the ion and create dark STIM contrast. The case where a grain is bright in both the SE and STIM images (e.g. the green rectangle in Fig. 1d and e) is unexpected and further investigation is required to explain this behaviour.

The datasets created by the position sensitive DLD detector allow the creation of images using the scattering angle as an imaging criterion. Hence, STIM images can be constructed using only the desired polar or azimuthal scattering angles, namely on-axis, off-axis or even an annular

ring. As different features in the image may scatter intensities differently because of their crystal orientations and/or chemical compositions, the possibility to form images with restricted scattering angle criterion offers an additional contrast mechanism that can be used in STIM imaging. To illustrate this, images of an area are shown in Fig. 2a-c which were formed only using intensities within the specified scattering angles (measured from the bright central spot on the detector). The detector image is shown in Fig. 2d. Each pixel represents an integer number of counts, any pixels with counts at or above the scale bar maximum are yellow, all other pixels have colours shown by the colour bar. These ranges were chosen to show the shape of the grains as well as the general spread of pixel values.

In order to understand the STIM images in the context of the crystallographic details of the sample, the crystal orientations of the exact same ROIs were mapped using the older and widely accepted TKD method. Representation of TKD data is a combination of inverse pole figure (IPF) in the colour channel and image quality (IQ) as grey value. For comparison, high-resolution BSE images were also obtained from the same ROIs. Selected sets of images in the three different imaging modes are shown in Fig. 3. These images reveal interesting differences stemming from the underlying variations in their contrast mechanisms. In the first row (Fig. 3a-c), both the STIM and TKD imaging modes show contrast between the left and the right side of the red box. However, the BSE mode fails to capture the contrast when the orientation changes. This could be because the change in orientation occurs below the relevant escape depth in the sample for the BSE mode to detect it, or it could be a case where these two different grain orientations happen to have the similar backscatter yield by coincidence. A tilt series with high

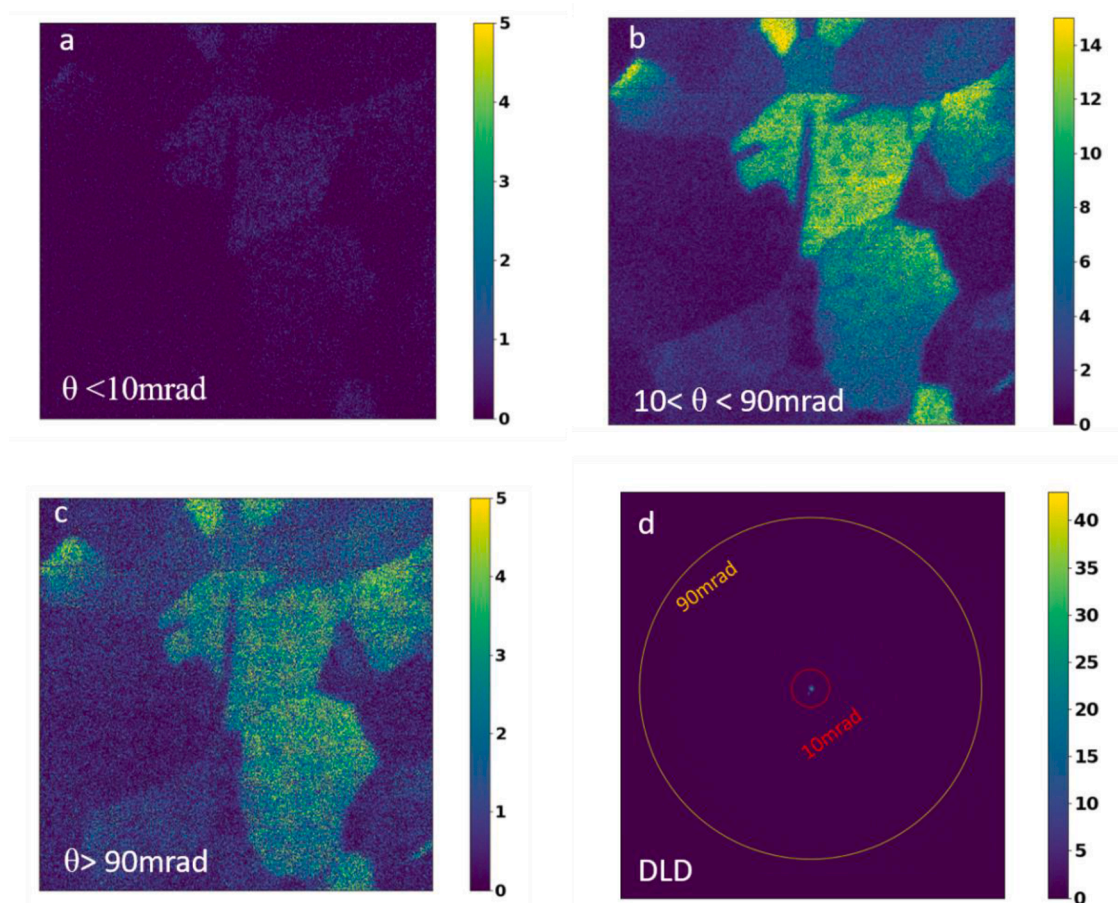


Fig. 2. (a-c) STIM images constructed using the specified scattering angles. (d) image of the DLD detector where the circles correspond to the scattering radii used for the STIM images. Areas of the sample that scatter intensities by different angles can produce image contrast. The field of view is $1.1\ \mu\text{m}$ for a-c. For colour images see the online version of this article.

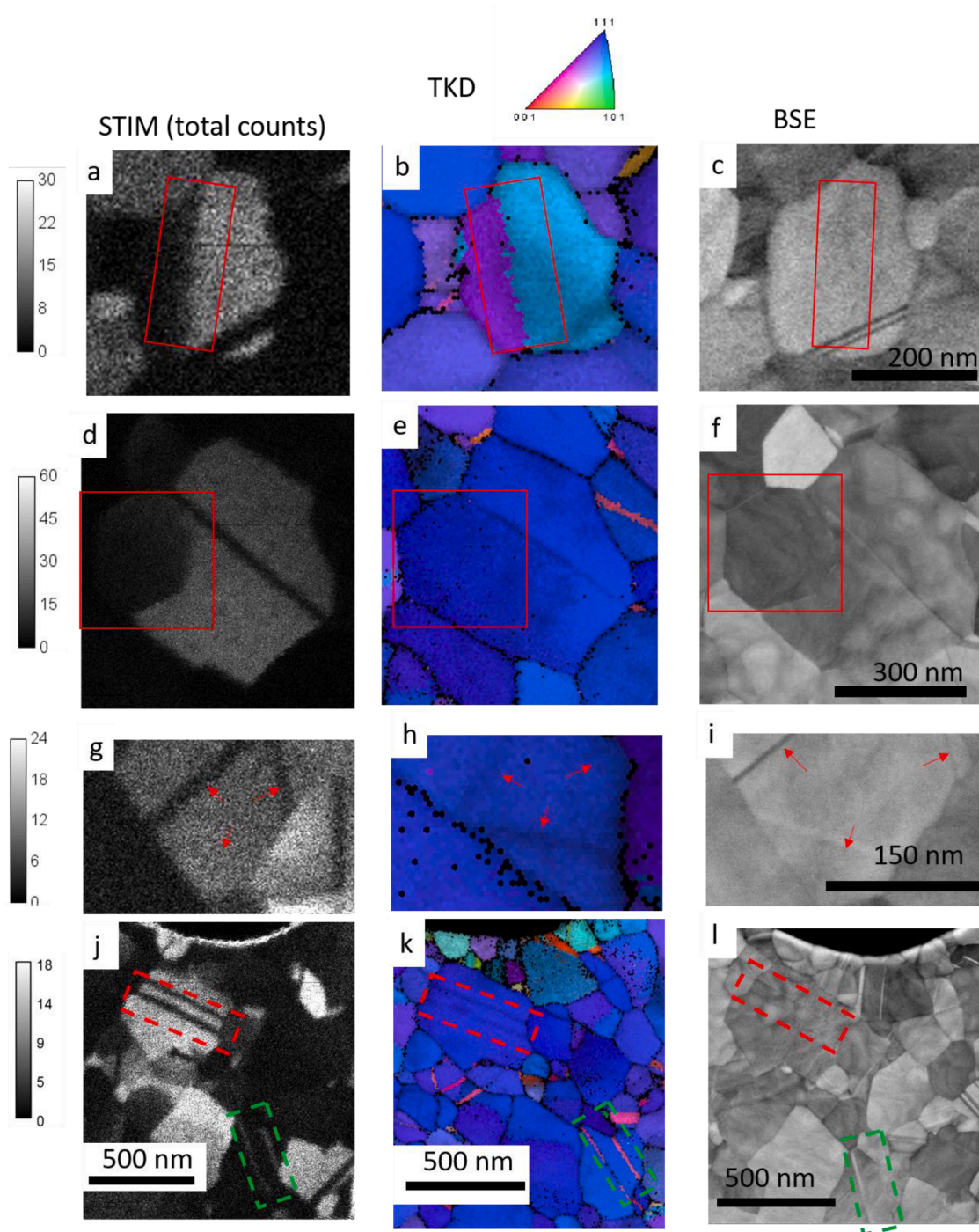


Fig. 3. Comparison of sets of images recorded in STIM, TKD and BSE modes. All images in a row are from the same area of the sample. Coloured boxes, arrows, and rectangles indicate features exhibiting differences in visibility or contrast depending on the imaging mode. The intensity range for the STIM images are provided next to the respective images. The grey levels in all the BSE images range from 0 (black) to 255 (white). For colour images see the online version of this article.

angular resolution or comparison with other techniques such as TEM could clarify this. Two parallel lines are seen in the central grain of the BSE image in Fig. 3c. They were identified as twin bands. Twin bands are typically bound by sets of $\{111\}$ planes of gold and as the film had a global $\{111\}$ fibre texture, the lines in the images trace $[110]$ direction. The two twin bands are clearly resolved in the BSE image. However, in the STIM image, they are visible but not separated. Similarly, in the TKD image there is a decrease in image quality due to Kikuchi pattern overlap, but the two bands are not resolved and there is no visible orientation contrast across the bands.

The second row (Fig. 3d-f) shows an example where a polygon

shaped grain on the top surface is apparent in BSE and STIM modes, but not visible in the TKD mode (see the red boxes). Similarly the shape of the brightest grain in Fig. 3f is not reproduced completely in the corresponding area in the TKD shown in Fig. 3e. In contrast to the clear line in the BSE, the top left edge is a collection of undetermined orientations in the TKD. To understand these effects, the following points need to be considered. Previous simulations[27] showed that for 30 keV electrons in Au, 80% of the final scattering events occur within an estimated distance of around 4 nm from the bottom surface. As the TKD is based on the diffraction pattern from the final scattering event of an electron within one thermal diffuse scattering mean free path of the lower surface

of the material, the 4 nm from the bottom surface can be considered as the information depth in the TKD images in Fig. 3. Any information from prior scattering events in the material is lost by subsequent elastic and inelastic scattering processes. Hence, the polygonal grain on the top surface is not captured in the TKD image. In contrast, the backscattered electron imaging gives information from the upper surface of the material. For 5 keV electrons in Au the information depth of the BSE signal can be estimated [28] to be around 21.5 nm from the top surface. Hence the polygonal grain on the top surface is visible in the BSE mode. This also explains the shape mismatch of the brightest grain in the BSE image in Fig. 3f and the corresponding TKD image as they are mainly a top view and bottom view of the sample respectively. It can be seen from the simulations that, for the 50 nm sample thickness in this study, there will be a central region where neither TKD nor BSE can provide information. As the STIM mode probes the entire thickness of the material, such information is present in the STIM image.

In the third row (Fig. 3g-i), a grain containing 3 twin bands is seen forming roughly 60° angle to one another (highlighted by the red arrows). These are pointing along the three variants of the $[110]$ directions and the twin bands are bound by sets of $\{111\}$ planes. It can be seen that each twin band appears differently, or not at all in each of the three imaging modes. Interestingly, the least visible twin band in BSE and TKD

is not the least visible in STIM. This will be further discussed later in Fig. 6.

In the fourth row (Fig. 3j-l), two grains with inverse contrasts are highlighted. Whilst in the grain marked by dashed red rectangles, the twin bands appear dark in a bright background, the opposite is observed in the grain marked by dashed green rectangles. The two twin bands within the red rectangles are visible in all three imaging modes although in the BSE image the contrast for the twins is relatively weak. On the other hand, the two twins within the green rectangles are visible in STIM and TKD images while only one of the twin bands is evident in the corresponding BSE image. This might be because the second twin happens to have the same backscatter yield as the parent grain or that the twin is present only on the bottom side of the sample. The latter situation, combined with the observed visibility of that twin in STIM, could suggest that the ions that first travel through unfavourable channelling orientation on the top crystal can be funnelled back into a channelling axis of a bottom crystal.

For all rows it can be seen that the low-voltage BSE has the highest resolution, exemplified by the double twin band in the lower right of the BSE image in row 1. For the STIM image this appears as only one band and it is hardly visible in the TKD image. In order to investigate this in more detail, a set of images taken in STIM, TKD and BSE modes all from

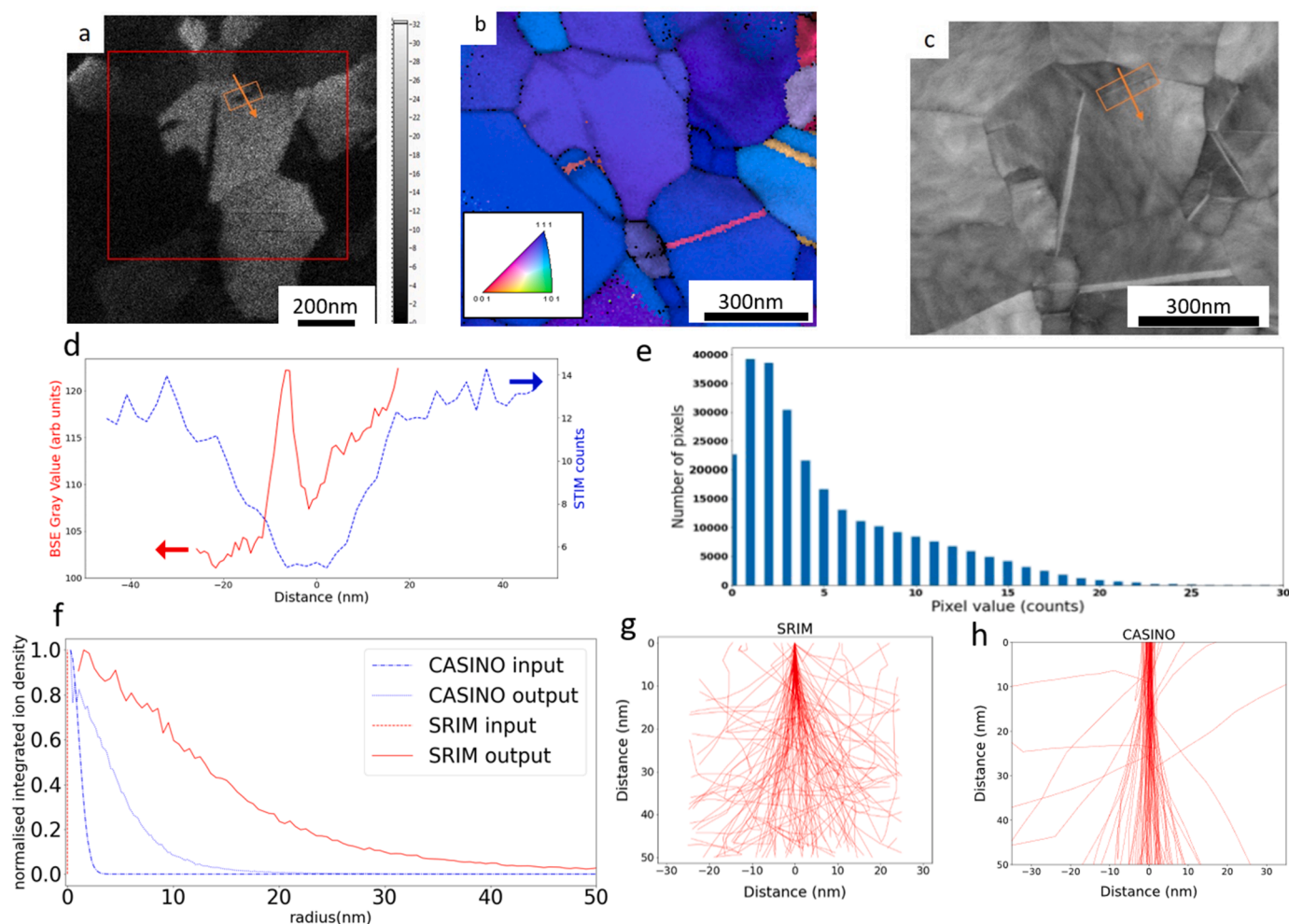


Fig. 4. Images of the same area recorded in STIM (a), TKD (b) and in BSE (c) modes. The inset in b shows the colour mapping for the different orientations. A comparison of the measured feature size for the same twin band in BSE and STIM is shown in (d). A histogram of the intensities of the STIM image in (a) is provided in (e). As the STIM intensities are absolute counts, the channelling efficiency across different parts of the image can be investigated quantitatively. The size of the ion and electron beams at the exit surface of the sample is shown in (f) alongside snapshots of ion and electron trajectories from SRIM and CASINO simulations respectively. Note also that the bright twin band seen in the bottom right of the BSE and the TKD images is not visible in the STIM image. For colour images see the online version of this article.

the same area are shown in Fig. 4a-c. Line profiles across the same twin band from BSE and STIM images are shown in Fig. 4d. A histogram of the STIM intensities in Fig. 4a is shown in Fig. 4e giving quantitative insights about the distribution of transmission channelling efficiencies within the imaged area. In order to evaluate the effect of beam broadening on the image resolutions, SRIM and CASINO simulations were performed and the beam radius at the exit surface of the sample for ion and electron beams are shown in Fig. 4f.

The differences in the image resolution can be partially explained by considering the broadening of the ion or electron beam in STIM and TKD respectively. In both cases, a nanometre-scale beam will be broadened to tens of nanometres. The SRIM results show that a 25 keV He beam spreads from a point to a full width half maximum (FWHM) of 26 nm when transmitting through 50 nm amorphous Au. Similarly, using CASINO software, a 30 keV electron beam of 2.6 nm FWHM ("probe size" parameter was 4.7 nm in the software) is spread to a FWHM of 8.3 nm when transmitted through 50 nm Au. These FWHM values are obtained from the integrated count density from radial histograms of the simulated trajectories. These spreads degrade the achievable resolution for both electrons and ions. In addition to the beam broadening, there is a reduced signal to noise ratio in the STIM mode reducing the image clarity. Furthermore, one must also consider that these twin bands are at an angle to the surface plane and, as such, when viewed normal to the plane they occupy a width, dependent on the film thickness, which would be wider than their actual width, even if an ideal probe was used. The two bands in the BSE image in Fig. 3c are of the order of 15 nm wide, and have a separation which is also around 15 nm. Features this close together were detectable but not resolvable by STIM. This was confirmed by a separate single feature which measured approximately 15 nm in BSE but gives a full width half maximum of 30 nm for the intensity dip in the STIM image (Fig. 4d). This matches with the observation that the two 15 nm features within about 15 nm of one another (as measured by BSE in Fig. 3c) were blurred into one on the STIM image. This also shows that for this STIM experimental setup the minimum resolvable twin band separation would be around 30 nm. Due to the inclination of the twin bands this is an overestimate for the best resolution. If the twin band was orientated parallel to the beam direction, the technique could resolve a narrower band.

Across the twin band within the orange box in Fig. 4a the average STIM counts per pixel drop from 14 to 5 counts/pixel (cf. Fig. 4d). This indicates that, for the collection angles of the full detector, and for this specific combination of orientations, the transmission efficiency ratio between the channelled and non-channelled ions is 2.8.

Now we discuss the factors that influence image contrast in the context of STIM imaging. When an ion reaches a channel (axial or planar), it will have a probability of being channelled which depends on the angle between the ion trajectory and the channel direction. A channel will have a specific range of angles for which channelling is most common, above a critical angle the ion has too much kinetic energy transverse to the channel direction and the crystal potential step of the channel sidewalls is no longer a sufficient barrier to redirect the ion. Previous experiments[29] have measured the full width half maximum for the transmitted intensity of 18 keV He⁺ in single crystal Au foils, as 6.04°, 5.81° and 4.63°, for the channels of the crystallographic directions <011>, <001> and <112>, respectively. The existence of a critical angle allows for strong contrast between different regions of a STIM image. Ions are only channelled by those regions of the sample with a channel direction orientated at an angle below this critical angle. These regions will appear bright because ions are effectively funnelled down the channels towards the detector, increasing the number of counts for that particular pixel. When the beam is positioned over an area with a channel direction orientated above the critical angle, efficient channelling does not occur. This means for the collection angles in this experiment, very few ions reach the detector, giving a darker pixel. When the beam direction is normal to the detector, and with all other factors equal, a larger misalignment angle between the ion beam

direction and the channel will decrease the intensity of the pixel for that raster position.

For the sample investigated in this paper, the thickness is uniform and so variations in transmission will be dominated by channelling effects. The intensity in the final STIM image of the sample will be mainly determined by the crystallographic orientation of the grains and defects in the Au film. The channelling efficiencies along different orientations show that indeed low index directions are favourable for channelling. Nevertheless, it is found that for orientations other than low index axis, channelling does occur but to a lower extent. This expected behaviour is consistent with the computational predictions[30,31]. This is an important reason why some twins are invisible in STIM images wherein, by coincidence, the orientations of the twin and the parent grain happen to align with two different, yet channelling directions resulting in poor or no contrast. Complete blocking of transmission or channelling away from the detector area occurred only very rarely, as can be seen in the histogram in Fig. 4e where the number of pixels with 0 intensity on the detector is a small fraction of the total 2.6×10^5 pixels in the STIM image.

Channelling was found to be sensitive not only to the grain orientations in the sample, but also to the imaging settings used. This is illustrated by the STIM images in Fig. 5 which were obtained at two different FOV sizes and the sample was not moved intentionally. As shown by the yellow boxes in Fig. 5, certain grains which were bright in the larger FOV (Fig. 5a, b) became darker in the smaller FOV (Fig. 5c), while for other grains the exact opposite effect was observed. The smaller FOV will have a higher ion dose than in the larger FOV. This is consistent with the higher counts seen in Fig. 5c than in Fig. 5a (and b). However, the higher dose can only explain higher counts, but it cannot explain the contrast reversal. Furthermore, as the sample was not moved, the local incidence angle would be exactly the same in Fig. 5b and c. Hence the contrast differences observed were not expected. We suspect either the sample had a minor drift and/or there is a small difference in the primary beam incidence angle when changing the FOV settings, both of which will influence channelling contrast.

The illustration in Fig. 6 provides a possible mechanism explaining why certain twins are dark in a bright grain while others are bright in a dark grain in the STIM images. The visibility of the twins may depend on their relative alignment of the twin boundaries with respect to the primary beam incidence angle. The twins with large areas of the twin boundaries exposed to the primary beam will be easily visible in STIM. If, by coincidence, twins and their parent grains happen to be orientated in two different yet channelling axes, there will be very little, or no channelling contrast and the twins remain invisible in the STIM images. A factor influencing channelling contrast is the convergence angle of the beam, which when increased, increases the spread in incidence angles between the ion and channel resulting in a loss of contrast and a reduction in peak brightness for the image. Detailed understanding of all the factors influencing channelling contrast is needed to perform more advanced experiments where ion energy losses upon traversing individual crystalline defects such as twins or stacking faults can be correlated to understand fundamental processes in ion-solid interaction with nanometre scale spatial resolution.

4. Conclusions

The channelling contrast across nanoscale twins in a thin gold membrane was analysed quantitatively by STIM. TKD and BSE images obtained from the same areas were used to correlate and understand the image contrast in STIM. For the experimental conditions used, a STIM lateral resolution of better than 30 nm was determined. The observed results were correlated with Monte Carlo simulations to derive insights related to beam broadening and the consequence in the STIM image resolution. Dark twins in bright grains and bright twins in dark grains were observed while some twins remained invisible in STIM. For the experimental conditions used, the ion transmission efficiency across a

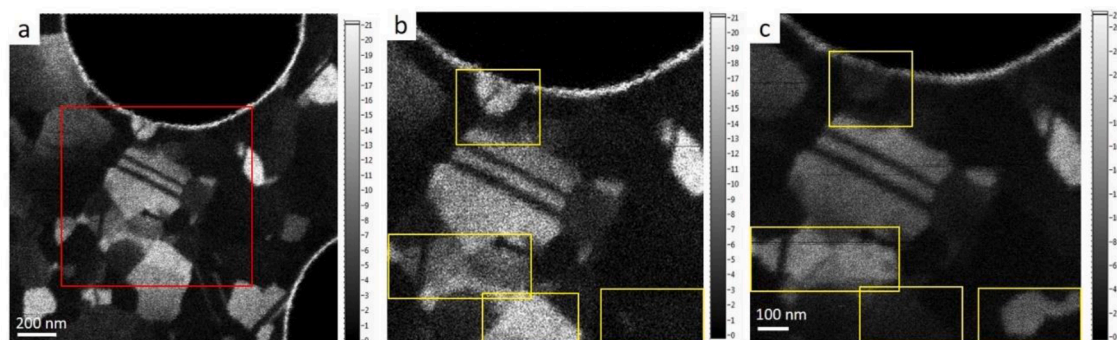


Fig. 5. Contrast reversals were observed for some grains upon changing the FOV settings. (a) and (c) are as-acquired images at two different FOVs. (b) is the same as (a) but cropped and enlarged to facilitate comparison with (c). Certain grains (e.g. bottom right), which are invisible in a larger FOV (a, b), appear clearly when a smaller FOV (c) is selected. The opposite effect is observed for some other grains (e.g. top centre). This indicates that the channelling contrast is sensitive to even small changes in the imaging conditions. For colour images see the online version of this article.

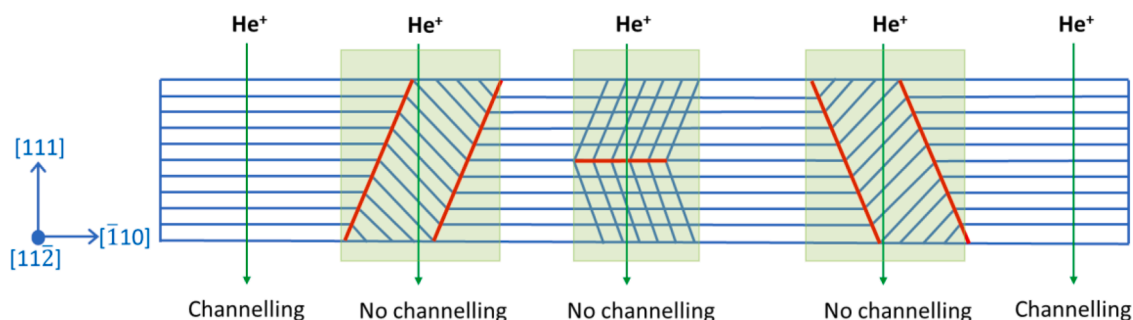


Fig. 6. Cross-sectional schematic to illustrate a few coherent twin variants within the sample. All the lines indicate (111) planes of gold. The red lines indicate the twin boundaries. When the incidence angle of the primary beam is aligned with the [111] direction of the grain, channelling is favoured, and the grain appears bright while the twins appear dark in the STIM image. Conversely, for reasons such as sample wrinkling, a condition can occur where the primary beam is aligned with the [111] of the twin which results in a bright twin in a dark grain in the STIM image (cf. Fig. 1a). If, by coincidence, a twin and its parent grain happen to align with two different channelling axes, they can be invisible in the STIM image (cf. Fig. 3g, i and Fig. 4a, c). For colour images see the online version of this article.

particular twin band was found to decrease by a factor of 2.8. Contrast reversal of some grains were observed suggesting the sensitivity of channelling contrast to even small differences in illumination conditions. A crystallographic analysis of the orientation of different twin variants was carried out to understand the contrast mechanisms involved in the imaging of twins. Moreover, it is suggested that when a twin and a parent grain happen to align with two different yet channelling axes, the twin can remain invisible in STIM. In general, STIM imaging contrast was excellent in comparison to conventional ion-induced SE imaging in HIM. This, combined with the fact that very low primary current is used in STIM (50 fA) in comparison to typical SE imaging in a HIM (few pA), implies that STIM imaging is a promising method for nanoscale imaging providing additional contrast mechanisms while potentially limiting beam induced sample damage in comparison to standard SE imaging in a HIM. This study demonstrates for the first time the possibility to investigate ion channelling within nanoscale structures such as isolated crystalline defects quantitatively. This opens the door for more advanced experiments such as analysing the ion energy loss characteristics with nanometre scale lateral resolution.

Declaration of Competing Interest

The authors declare that they have no known competing financial interests or personal relationships that could have appeared to influence the work reported in this paper.

Acknowledgements

This work was funded by the Luxembourg National Research Fund (FNR) by the grants PRIDE17/12246511/PACE and STHIM (C16/MS/11354626). This project also received funding from the European Union's Horizon 2020 Research and Innovation Programme under grant agreement No. 720964.

References

- [1] Helium ion microscopy, in: G. Hlawacek, A. Götzhäuser (Eds.), *Springer Tracts in Modern Physics*, 272, Springer, 2018.
- [2] V. Sidorkin, et al., Sub-10-nm nanolithography with a scanning helium beam, *J. Vac. Sci. Technol. B Microelectron. Nanom. Struct.* 27 (2009), L18.
- [3] D. Dowsett, T. Wirtz, Co-Registered In Situ Secondary Electron and Mass Spectral Imaging on the Helium Ion Microscope Demonstrated Using Lithium Titanate and Magnesium Oxide Nanoparticles, *Anal. Chem.* 89 (2017) 8957–8965.
- [4] N. Klingner, R. Heller, G. Hlawacek, S. Facsko, J. von Borany, Time-of-flight secondary ion mass spectrometry in the helium ion microscope, *Ultramicroscopy* 198 (2019) 10–17.
- [5] M.G. Stanford, B.B. Lewis, K. Mahady, J.D. Fowlkes, P.D. Rack, Review Article: advanced nanoscale patterning and material synthesis with gas field helium and neon ion beams, *J. Vac. Sci. Technol. B, Nanotechnol. Microelectron. Mater. Process. Meas. Phenom.* 35 (2017), 030802.
- [6] R. Van Gastel, G. Hlawacek, S. Dutta, B. Poelsema, Backscattered helium spectroscopy in the helium ion microscope: principles, resolution and applications, *Nucl. Instrum. Methods Phys. Res. Sect. B Beam Interact. with Mater. Atoms* 344 (2015) 44–49.
- [7] N. Klingner, et al., Nanometer scale elemental analysis in the helium ion microscope using time of flight spectrometry, *Ultramicroscopy* 162 (2016) 91–97.
- [8] V. Veligura, G. Hlawacek, R. VanV. Gastel, H.J.W. Zandvliet, B. Poelsema, A high resolution ionoluminescence study of defect creation and interaction, *J. Phys. Condens. Matter* 26 (2014), 165401.
- [9] T. Wirtz, O. De Castro, J.-N. Audinot, P. Philipp, Imaging and Analytics on the Helium Ion Microscope, *Annu. Rev. Anal. Chem.* 12 (2019) 1–21.

- [10] J.A. Notte, et al., Diffraction imaging in a He⁺ ion beam scanning transmission microscope, *Microsc. Microanal.* 16 (2010) 599–603.
- [11] E. Serralta, et al., Scanning transmission imaging in the helium ion microscope using a microchannel plate with a delay line detector, *Beilstein J. Nanotechnol.* 11 (2020) 1854–1864.
- [12] L. Scipioni, C.A. Sanford, J. Notte, B. Thompson, S. McVey, Understanding imaging modes in the helium ion microscope, *J. Vac. Sci. Technol. B Microelectron. Nanom. Struct.* 27 (2009) 3250.
- [13] L.P. Zweifel, I. Shorubalko, R.Y.H. Lim, Helium Scanning Transmission Ion Microscopy and Electrical Characterization of Glass Nanocapillaries with Reproducible Tip Geometries, *ACS Nano* 10 (2016) 1918–1925.
- [14] D. Emmrich, et al., Scanning transmission helium ion microscopy on carbon nanomembranes, *Beilstein J. Nanotechnol.* 12 (2021) 222–231.
- [15] J. Wang, et al., Focussed helium ion channeling through Si nanomembranes, *J. Vac. Sci. Technol. B, Nanotechnol. Microelectron. Mater. Process. Meas. Phenom* 36 (2018), 021203.
- [16] K.L. Kavanagh, C. Herrmann, J.A. Notte, Camera for transmission He⁺ ion microscopy, *J. Vac. Sci. Technol. B, Nanotechnol. Microelectron. Mater. Process. Meas. Phenom* 35 (2017), 06G902.
- [17] Kavanagh, K.L., Bunevich, A. & Motapothula, M.R. **Transmission Helium Ion Microscopy of Graphene.** <http://arxiv.org/abs/2004.01682> (2020).
- [18] T.J. Woehl, R.M. White, R.R. Keller, Dark-Field Scanning Transmission Ion Microscopy via Detection of Forward-Scattered Helium Ions with a Microchannel Plate, *Microsc. Microanal.* 22 (2016) 544–550.
- [19] M. Mousley, et al., Stationary beam full-field transmission helium ion microscopy using sub-50keV He⁺: projected images and intensity patterns, *Beilstein J. Nanotechnol.* 10 (2019) 1648–1657.
- [20] O. De Castro, et al., npSCOPE: a New Instrument Combining SIMS Imaging, SE Imaging and Transmission Ion Microscopy for High Resolution In-situ Correlative Investigations, *Microsc. Microanal.* 26 (2020) 1976–1977.
- [21] N. Brodusch, H. Demers, R. Gauvin, Nanometres-resolution Kikuchi patterns from materials science specimens with transmission electron forward scatter diffraction in the scanning electron microscope, *J. Microsc.* 250 (2013) 1–14.
- [22] P.W. Trimby, et al., Characterizing deformed ultrafine-grained and nanocrystalline materials using transmission Kikuchi diffraction in a scanning electron microscope, *Acta Mater* 62 (2014) 69–80.
- [23] P.W. Trimby, Orientation mapping of nanostructured materials using transmission Kikuchi diffraction in the scanning electron microscope, *Ultramicroscopy* 120 (2012) 16–24.
- [24] Ziegler, J.F., Ziegler, M.D. & Biersack, J.P. **SRIM – The Stopping and Range of Ions in Matter** (2010). (2010).
- [25] CASINO. <https://www.gel.usherbrooke.ca/casino/index.html>.
- [26] V. Veligura, G. Hlawacek, R. Van Gastel, H.J.W. Zandvliet, B. Poelsema, Channeling in helium ion microscopy: mapping of crystal orientation, *Beilstein J. Nanotechnol.* 3 (2012) 501–506.
- [27] R. van Bremen, D. Ribas Gomes, L.T.H. de Jeer, V. Ocelík, J.T.M. De Hosson, On the optimum resolution of transmission-electron backscattered diffraction (t-EBSD), *Ultramicroscopy* 160 (2016) 256–264.
- [28] J. Piños, Mikmeková, L Frank, About the information depth of backscattered electron imaging, *J. Microsc.* 266 (2017) 335–342.
- [29] C.J. Andreen, R.L. Hines, Critical angles for channeling of 1- to 25-keV H⁺, D⁺, and He⁺ ions in gold crystals, *Phys. Rev.* 159 (1967) 285–290.
- [30] S. Ghaderzadeh, M. Ghorbani-Asl, S. Kretschmer, G. Hlawacek, A. V. Krashenninikov, Channeling effects in gold nanoclusters under He ion irradiation: insights from molecular dynamics simulations, *Nanotechnology* 31 (2020).
- [31] K. Nordlund, F. Djurabekova, G Hobler, Large fraction of crystal directions leads to ion channeling, *Phys. Rev. B* 94 (2016).